Q. J. R. Meteorol. Soc. (2006), **132**, pp. 101–124 doi: 10.1256/qj.04.145

Boundary-layer friction in midlatitude cyclones

By D. S. ADAMSON, S. E. BELCHER, B. J. HOSKINS and R. S. PLANT*

SUMMARY

Results from an idealized three-dimensional baroclinic life-cycle model are interpreted in a potential vorticity (PV) framework to identify the physical mechanisms by which frictional processes acting in the atmospheric boundary layer modify and reduce the baroclinic development of a midlatitude storm. Considering a life cycle where the only non-conservative process acting is boundary-layer friction, the rate of change of depth-averaged PV within the boundary layer is governed by frictional generation of PV and the flux of PV into the free troposphere. Frictional generation of PV has two contributions: *Ekman generation*, which is directly analogous to the well-known Ekman-pumping mechanism for barotropic vortices, and *baroclinic generation*, which depends on the turning of the wind in the boundary layer and low-level horizontal temperature gradients. It is usually assumed, at least implicitly, that an Ekman process of negative PV generation is the mechanism whereby friction reduces the strength and growth rates of baroclinic systems. Although there is evidence for this mechanism, it is shown that baroclinic generation of PV dominates, producing positive PV anomalies downstream of the low centre, close to developing warm and cold fronts. These PV anomalies are advected by the large-scale warm conveyor belt flow upwards and polewards, fluxed into the troposphere near the warm front, and then advected westwards relative to the system. The result is a thin band of positive PV in the lower troposphere above the surface low centre. This PV is shown to be associated with a positive static stability anomaly, which Rossby edge wave theory suggests reduces the strength of the coupling between the upper- and lower-level PV anomalies, thereby reducing the rate of baroclinic development. This mechanism, which is a result of the baroclinic dynamics in the frontal regions, is in marked contrast with simple barotropic spin-down ideas. Finally we note the implications of these frictionally generated PV anomalies for cyclone forecasting.

KEYWORDS: Baroclinic generation Cyclogenesis Potential vorticity Static stability Surface drag

1. INTRODUCTION

Accurate representation of surface drag is an important aspect of numerical weather prediction (NWP). For example, subgrid-scale hills enhance the drag (Wood and Mason 1993; Belcher and Hunt 1998; Beljaars *et al.* 2004), and the inclusion of this orographic roughness has been shown to improve significantly NWP forecast skill (Milton and Wilson 1996). Other sources of enhanced drag occur for stably stratified flow around hills (Lott and Millar 1997) and during the growth of ocean surface waves (Janssen 1989, 1991). Doyle (1995) found that the increased drag due to coupling with ocean waves improved medium-range forecasts of low-level winds and surface pressure minima. A common thread that emerges from these studies is that physically motivated changes to the formulation of drag are beneficial for NWP. However, the actual mechanisms through which surface drag affects synoptic-scale processes are not well understood. The aim of this paper is to pursue this general question by focusing on understanding the role of boundary-layer friction within developing midlatitude baroclinic cyclones.

There is clear evidence that boundary-layer friction does change baroclinic cyclones. Valdes and Hoskins (1988) investigated the baroclinic instability of a zonal-mean flow and found that surface drag can reduce the growth rates of baroclinic systems by 50%. Similar reductions to large-scale eddy kinetic energies were found in the baroclinic life-cycle study of Jones (1992). But what are the physical mechanisms that produce these changes?

* Corresponding author: Department of Meteorology, University of Reading, PO Box 243, Reading, Berkshire RG6 2BB, UK. e-mail: r.s.plant@rdg.ac.uk

It is well known that a homogeneous barotropic circulation is affected by surface drag through Ekman pumping. Accordingly, beneath a cyclonic circulation, boundary-layer friction leads to convergence which, by mass continuity, induces vertical transport out of the boundary layer at the centre of the circulation. The vertical transport gradient then decreases the vorticity and thus Ekman pumping tends to spin down the circulation above the boundary layer (e.g. Holton 1992). (Within the boundary layer this secondary circulation partially offsets the direct reduction of vorticity caused by the frictional reduction in wind speed.) Some idealized models of baroclinic systems (such as Card and Barcilon 1982; Farrell 1985) have parametrized the effects of the atmospheric boundary layer by specifying at the bottom boundary a vertical velocity derived from Ekman pumping. This practice suggests an (often implicit) assumption that Ekman pumping is the main effect of boundary-layer drag on baroclinic systems, despite the theory being developed only for barotropic systems.

The action of Ekman pumping in a barotropic vortex is understood in terms of vorticity dynamics. The natural generalization for baroclinic systems is potential vorticity (PV), defined by $P = \rho^{-1}\,\boldsymbol{\zeta} \cdot \nabla\theta$, where ρ, $\boldsymbol{\zeta}$ and θ are density, vorticity and potential temperature, respectively. This quantity is central in synoptic-scale dynamics, particularly in the development of baroclinic systems (Hoskins *et al.* 1985). PV is materially conserved under inviscid, adiabatic conditions, but changes under the action of friction (such as generated by turbulence in the atmospheric boundary layer) or diabatic heating (such as produced by moist convection). According to the impermeability theorem of Haynes and McIntyre (1987), the mass-weighted PV between two isentropes can only change when the isentropes intersect a boundary. Thus, we expect the boundary layer at the earth's surface to be a source of any net changes in PV.

Baroclinic instability can be understood as a cooperative interaction between PV anomalies (Hoskins *et al.* 1985), one at the earth's surface associated with a surface temperature gradient (Bretherton 1966; Schneider *et al.* 2003) and the other associated with an interior anomaly (Methven *et al.* 2004), particularly near the steering level*. The question then arises as to how frictional processes within the boundary layer generate PV and affect its evolution (and hence affect cyclone development).

Using a two-dimensional (2D) inviscid model of frontogenesis, Nakamura and Held (1989) showed that occlusion of frontal surfaces enables PV to be extruded into the troposphere from the reservoir associated with the surface temperature gradient. This PV is associated with high static stability, and so reduces the coupling between the surface and tropopause anomalies. However, Cooper *et al.* (1992) argued that any such effect from occlusion is of minor importance in the presence of frictional and diabatic processes. They showed that in a 2D Eady model with a boundary-layer parametrization, there are mechanisms (which are discussed in section 5) whereby turbulent fluxes of heat and momentum produce significant irreversible changes to the PV prior to frontal occlusion. According to the 2D model of Xu *et al.* (1998), Ekman transport pumps the generated PV away from the boundaries and into the troposphere. A shallow boundary-layer circulation induced by the Ekman pumping then produces horizontal spreading of the anomalous PV above the boundary layer.

The restriction to modelling two dimensions clearly limits the possible transports of PV generated within the boundary layer in these studies. PV generation by friction in a 3D system, for a case-study of marine cyclogenesis, was considered by Stoelinga (1996). The synoptic situation was complicated considerably beyond the studies discussed above owing to the use of a full mesoscale model, and in particular to the significant

* Longer waves also have a maximum near the tropopause.

generation of PV by latent heating. Nonetheless, careful partitioning of the PV generation allowed for the identification of some low-level positive PV, attributable to surface drag, mainly in the easterly flow in the warm frontal zone. Inversion of the PV structure resulted in a small cyclonic circulation close to the surface low, thus enhancing the low-level vorticity. Davis *et al.*'s (1993) analysis of a continental cyclone also showed significant net positive PV generation by friction, primarily generated to the north of the warm front. However, in both studies the overall effect of surface drag was to give a weaker low-level cyclone (dramatically so in the continental case), apparently because of reduced development of the upper-tropospheric anomaly. Thus, 'the complete role of (surface friction) may be much more complicated than the spin-down of an isolated vortex' (Davis *et al.* 1993).

The discussion above leaves important questions unanswered. First, how are the PV generation mechanisms identified by Cooper *et al.* (1992) expressed in a 3D baroclinic wave? Second, what is the relative importance of each mechanism? Third, where is the PV generated by boundary-layer friction transported? And fourth, how does the frictional modification of PV inhibit the development of the low-level cyclone? We address these issues here by performing 3D simulations of the life cycle of an idealized baroclinic wave, with a full representation of boundary-layer friction. We consider both the frictional PV generation and its subsequent transport.

The remainder of this paper is structured as follows: Section 2 describes the life-cycle model, with particular attention being given to the representation of surface drag and turbulent vertical momentum fluxes. The effects of drag on the life cycle are presented in sections 3 and 4, the latter describing the low-level PV evolution. Sections 5(a), (b) consider the equations governing PV, including the balance between the frictional generation of PV, the depth-averaged boundary-layer PV and the flux of PV into the free troposphere. The simulation results are then considered from this PV perspective in sections 5(c), (d) and this leads to the proposal of a mechanism by which surface drag acts to reduce baroclinic growth rates (section 6).

2. The Reading IGCM

The Reading Intermediate General Circulation Model (IGCM) is a simplified model of the general circulation based on the global, primitive-equation model of Hoskins and Simmons (1975). It represents atmospheric variables as a truncated series of spherical harmonics in the horizontal and on sigma levels in the vertical. A description of the equation sets used, their method of solution and the overall model structure can be found in Hoskins and Simmons (1975) and Methven (1996).

An inviscid, adiabatic form of the model has successfully been used in a number of studies of dry baroclinic life cycles. For example, Simmons and Hoskins (1978, 1980) investigated the life-cycle behaviour for normal modes with various wave-number symmetries and for a range of initial states with different zonal jets. Some general features of the life cycles were found to be robust; for example, in each case a period of baroclinic growth and cyclone development was followed by a period of barotropic decay. However, wave-number-six symmetry produced characteristics that were most representative of real cyclones and has therefore been adopted here.

The initial state and normal mode chosen here were collectively referred to as the LC1 life cycle by Thorncroft *et al.* (1993). The initial state is zonally symmetric, with a westerly jet of 47 m s^{-1} centred at 43°N and a corresponding surface temperature difference of 40 K between 30 and 60°N (Thorncroft *et al.* 1993, their Fig. 3a). To assist with the later identification of anomalous PV, Fig. 1 shows the initial-state PV averaged

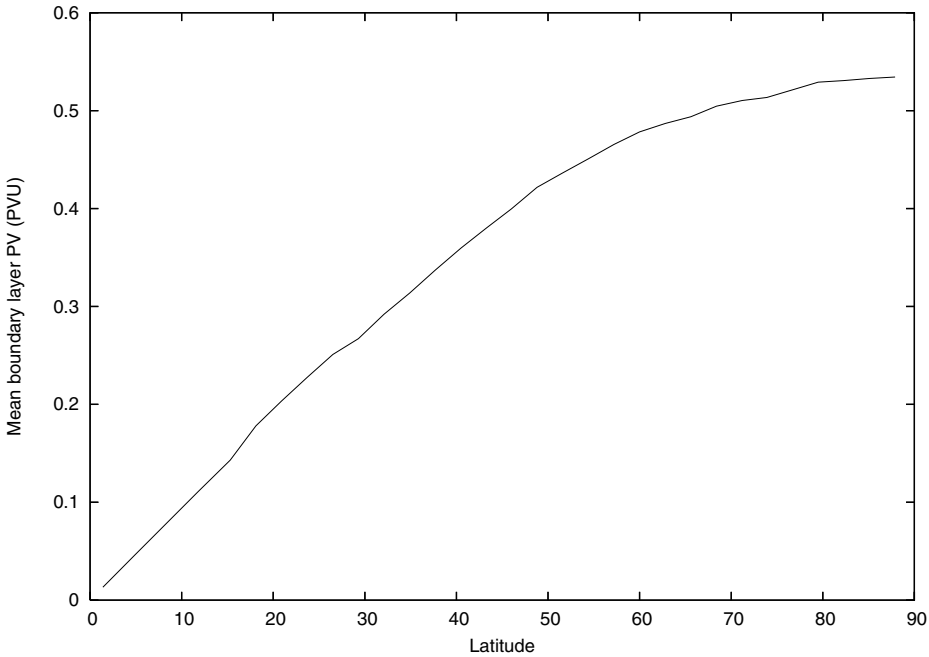

Figure 1. The depth-averaged potential vorticity (PV units) in the boundary layer in the initial state as a function of latitude. The initial state has zonal symmetry.

over the boundary layer (up to $\sigma = 0.92$, as defined in section 5(c)). The life cycle is initiated by adding the fastest-growing normal mode at wave number six to the basic state, the mode having been normalized to give a surface pressure perturbation of 1 mb.

A resolution of T42 L19 is used here. Experiments with LC1 at T213 (Adamson 2001) show good agreement with the T42 results, which are sufficient for the present purposes. However, it is desirable to have good vertical resolution within the boundary layer for this study (Adamson 2001) and so we include extra levels there in comparison with the 15 vertical levels used by Simmons and Hoskins (1980) and Thorncroft *et al.* (1993). The new levels improve the near-surface grid spacing to between 100 and 200 m.

Previous studies have shown that the dynamics of the IGCM are sufficient to capture many of the important features of cyclone development, but within a relatively simple model when compared to full NWP models. The simulations to be discussed are dry and exclude diabatic processes such as surface heat fluxes, convection and radiation*. This approach ensures that PV is conserved above the boundary layer and so enables the spatial evolution of frictionally generated PV anomalies to be clearly identified.

(*a*) *IGCM boundary-layer scheme*

The boundary-layer scheme implemented in the IGCM is based on the mixing-length approach of Louis (1979) and Louis *et al.* (1982). A highly sophisticated scheme is not warranted for this application and the intention is to take a relatively simple but reasonable approach. Nonetheless, the scheme is broadly similar to that used in the ECMWF forecast model (A. Beljaars, personal communication).

* We intend to report on the effects of diabatic processes in the near future.

The lowest model level is assumed to lie within the surface layer, so that the surface stress can be represented by the bulk aerodynamic formula

$$\boldsymbol{\tau}_{\mathrm{s}} = \rho C_{\mathrm{D}} |\mathbf{v}_1| \mathbf{v}_1, \tag{1}$$

where $\mathbf{v}_1$ is the horizontal wind on the lowest model level. Under neutral conditions the drag coefficient C_{D} is directly related to the surface roughness. Since most baroclinic cyclogenesis occurs over the ocean, we determine suitable roughness lengths from a Charnock relation (ECMWF Research Department 1991),

$$z_{0\mathrm{m}} = \max\left(\alpha_{\mathrm{c}} \frac{u_*^2}{g},\, 1.15 \times 10^{-5}\right), \tag{2}$$

with $\alpha_{\mathrm{c}} = 0.018$ and the friction velocity u_* being taken from its value for the previous time step. In addition, the drag coefficient varies with surface-layer stability according to Monin–Obukhov similarity theory. (The surface temperature is held constant in time. It affects the interior flow only through the surface-layer stability.) The flux profiles used to account for such variation are those recommended for 'most practical applications' by Arya (1988), viz.

$$\phi_{\mathrm{m}} = \begin{cases} 1 + 5\dfrac{z}{L_{\mathrm{MO}}} & \text{for } \dfrac{z}{L_{\mathrm{MO}}} > 0 \\ \left(1 - 15\dfrac{z}{L_{\mathrm{MO}}}\right)^{-1/4} & \text{for } \dfrac{z}{L_{\mathrm{MO}}} < 0, \end{cases} \tag{3}$$

where ϕ_{m} is the non-dimensionalized shear and z is height. At each time step, the Monin–Obukhov length L_{MO} and drag coefficient are computed iteratively until convergence to within 0.5% is achieved.

Above the lowest model level, boundary-layer stress is written in terms of a mixing length:

$$\boldsymbol{\tau} = -\rho K_{\mathrm{m}} \frac{\partial \mathbf{v}}{\partial z}; \quad K_{\mathrm{m}} = l_{\mathrm{m}}^2 \left|\frac{\partial \mathbf{v}}{\partial z}\right| f_{\mathrm{m}}(Ri). \tag{4}$$

The mixing length, l_{m}, is represented by an adaptation of the Blackadar (1962) formula,

$$l_{\mathrm{m}}^{-1} = (\kappa z)^{-1} + (l_0 \beta)^{-1}, \tag{5}$$

where $l_0 = 150$ m (ECMWF Research Department 2002) and κ is the von Kármán constant. The factor β is introduced to reduce the mixing length for large heights, preventing strong vertical diffusion in the vicinity of the tropospheric jet and so avoiding the necessity to impose a cap on the boundary layer. It is given by

$$\beta = \beta_0 + \frac{1 - \beta_0}{1 + (z/H)^2}, \tag{6}$$

where $\beta_0 = 0.2$ and $H = 4000$ m (ECMWF Research Department 2002). It remains to define the function $f_{\mathrm{m}}(Ri)$ from Eq. (4). This function of the Richardson number represents the dependence of the eddy diffusivity on atmospheric stability (Louis 1979) and is given by

$$f_{\mathrm{m}} = \begin{cases} \dfrac{1}{1 + 2b\,Ri(1 + d\,Ri)^{-1/2}} & \text{for } Ri \geqslant 0 \\ 1 - \dfrac{2b\,Ri}{1 + 3bc\sqrt{-Ri}\,(l_{\mathrm{m}}/z)^2\, 3^{-3/2}} & \text{for } Ri < 0 \end{cases} \tag{7}$$

with $b = c = 5$ (Louis *et al.* 1982; ECMWF Research Department 1991) and $d = 1$ (Viterbo *et al.* 1999; ECMWF Research Department 2002).

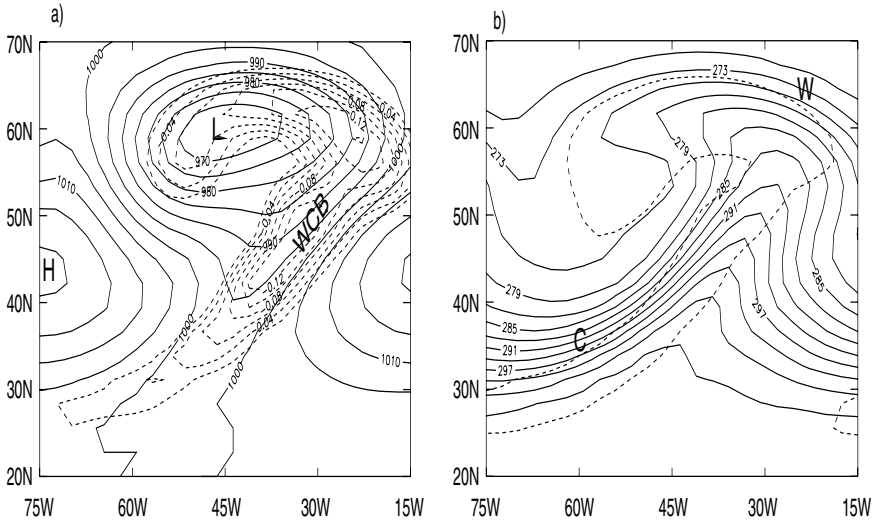

Figure 2. The life cycle Rd after seven days: (a) surface pressure (solid, contour interval 5 mb), with L and H denoting the surface low and high pressure centres and WCB the warm conveyor belt region, and the ascent rate ω (contour interval 0.02 Pa s^{-1}, shown dashed for negative values only) on the surface $\sigma = 0.92$, and (b) potential temperature (solid, contour interval 3 K) at $\sigma = 0.92$, and the 10^{-5} s^{-1} relative vorticity contour (dashed) at $\sigma = 0.995$, with W and C denoting the warm and cold fronts.

3. Life cycle with drag

The effects of drag have been investigated by comparing a simulation R0 (where the model is run without the boundary-layer formulation), with a simulation Rd which includes the boundary-layer formulation described above, but has no diabatic processes (other than numerical hyperdiffusion).

Let us briefly review the evolution of the baroclinic life cycle. In both cases, this begins with three days of almost linear* baroclinic growth, high and low pressure centres developing at ~50°N. This is followed by five or six days of nonlinear baroclinic growth, during which time the high pressure region migrates equatorwards and the low pressure region polewards. The low centre moves eastwards at ~14 m s^{-1} (slightly slower with drag included). Figure 2 shows the surface isobars after seven days of the run Rd, along with the low-level ascent, relative vorticity and potential temperature. At this stage, warm (W) and cold (C) fronts can be clearly distinguished. In both runs, warm air moves northwards and ascends ahead of and parallel to the surface cold front. This flow is termed the warm conveyor belt (WCB) and transports warm low-latitude air near the surface, upwards and polewards to higher latitudes, overrunning colder air at the warm front. The WCB splits in the region of the warm front (Browning and Roberts 1994), with air on the underside of the WCB moving cyclonically westwards relative to the system, towards the low centre. This branch of the flow is important for the transport of PV anomalies (sections 4 and 5(c)). After around ten days, the surface pressure anomalies decay and vertical motion decreases.

Inclusion of the boundary-layer scheme has two main effects on the evolution of the system. First, cyclone intensity is substantially reduced, the maximum surface pressure perturbation for the low decreasing from 70 to 37 mb. The reduction in the total intensity of the high–low pressure dipole can be seen from the evolution of the domain-averaged eddy kinetic energy (Fig. 3).

* In terms of the relative vorticity maximum or the size of the pressure perturbation for instance.

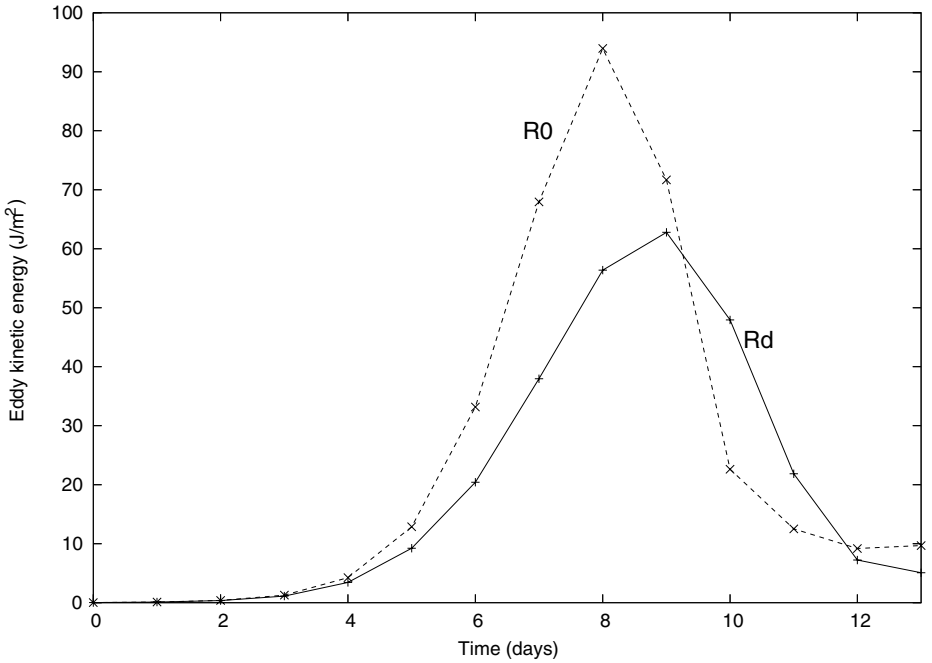

Figure 3. The domain-averaged eddy kinetic energy during life cycles R0 and Rd.

Figure 3 also reveals the second main effect of drag, which is to introduce a delay in the life-cycle evolution. The pattern of energy conversions in the two simulations is similar. During the period of baroclinic growth, zonal-mean potential energy associated with the basic state is converted via eddy potential energy into eddy kinetic energy. This is followed by a period of barotropic decay, in which the eddy kinetic energy is converted into zonal-mean kinetic energy. Surface drag reduces both conversion rates. Weaker baroclinic conversions lead to slower growth of the eddy, but there is some compensation in that a weaker barotropic decay allows for development to persist for longer. This results in a lag in the maximum eddy kinetic energy by about a day and a reduction of $\sim$35% in that maximum.

A damped and delayed evolution with drag included can be seen in the evolution of various other variables, such as the low-level potential temperature, vertical velocity and relative vorticity. The remainder of this paper adopts a PV framework for determining the mechanisms by which drag affects these changes to the baroclinic dynamics.

4. Low-level PV in the baroclinic life cycles

For the first few days of the frictionally damped run Rd, low-level PV anomalies are small. However, as the cyclone develops into a stronger system, significant anomalies are produced, not dissimilar to the structures seen by Stoelinga (1996, his Fig. 7(d)). After around four days, a positive PV anomaly develops on the eastern flank of the developing low, near the base of the boundary layer (location P1 in Fig. 4). Over the next four days, both the cyclone and this positive anomaly strengthen rapidly, and distinct warm and cold fronts form on the north-eastern and southern flanks of the low centre respectively (Fig. 2). A negative PV anomaly also develops close to the surface low centre.

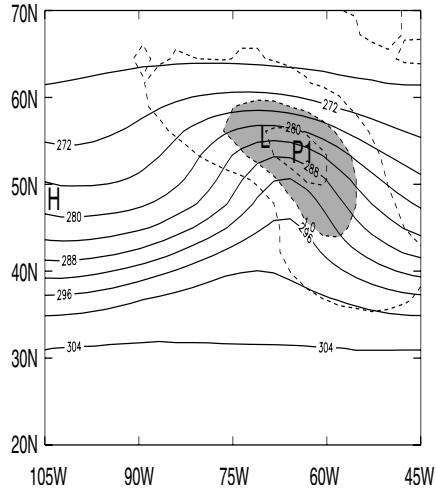

Figure 4. Potential temperature (solid, contour interval 4 K) and potential vorticity (dashed, contour interval 0.5 PVU, with values >1 PV units shaded) on the surface $\sigma = 0.98$ in run Rd after four days. L and H denote the surface low and high pressure centres, and location P1 is described in the text.

Figure 5 shows the PV within and just above the boundary layer after six days of the run Rd. The negative anomaly (labelled as N) can be first distinguished around this time, close to the surface, in Fig. 5(a). It intensifies over the next few days and extends a little higher, but remains an isolated structure at the base of the boundary layer in the vicinity of the low (see Fig. 6, which shows this anomaly after eight days). As we discuss in section 5(c), this anomaly is associated with Ekman pumping, operating at and just ahead of the low centre. Beyond nine days the negative anomaly is diluted as the cyclone decays, the structure becoming difficult to discern after about thirteen days. This can be seen in Fig. 7, which shows the maximum and minimum values of PV that occur on levels corresponding to the positive and negative anomalies respectively.

We turn now to the positive low-level anomaly. At early times, it is formed near the base of the boundary layer (Fig. 4). During later development, the positive anomaly P1 close to the surface migrates southwards to occupy a region of strong poleward advection ahead of the northern portion of the developing cold front (Fig. 5(a)), a position it maintains as the cyclone approaches maturity (Fig. 6). Moreover, the anomaly extends throughout the boundary layer and a little above, with the shape and location of the anomaly changing considerably with height (Fig. 5). Animations of the PV field and qualitative tracing of trajectories show that the near-surface region acts as a source of anomalous PV. The generated PV is advected north-eastwards along the WCB (Fig. 2) ahead of the low centre. As it does so, the PV ascends (Figs. 5(b) and (c)). Note that the WCB becomes increasingly pronounced during cyclone development and so the ascent is correspondingly enhanced between the fourth and eighth days. Upon reaching the vicinity of the warm front, further advection takes place predominantly along the cyclonic branch of the WCB (section 3). Thus, the PV is transported westwards relative to the cyclone, towards the low centre. The result is a positive PV anomaly, located towards the top of the boundary layer and then later also in the lower part of the free troposphere. Figure 8 shows an east–west cross-section through this elevated part of the positive anomaly. Between six and eight days the anomaly expands in the vertical.

After about eight days, the PV in an additional region also becomes apparent (Fig. 6); anomalous positive PV values, labelled as P2, are found close to the surface

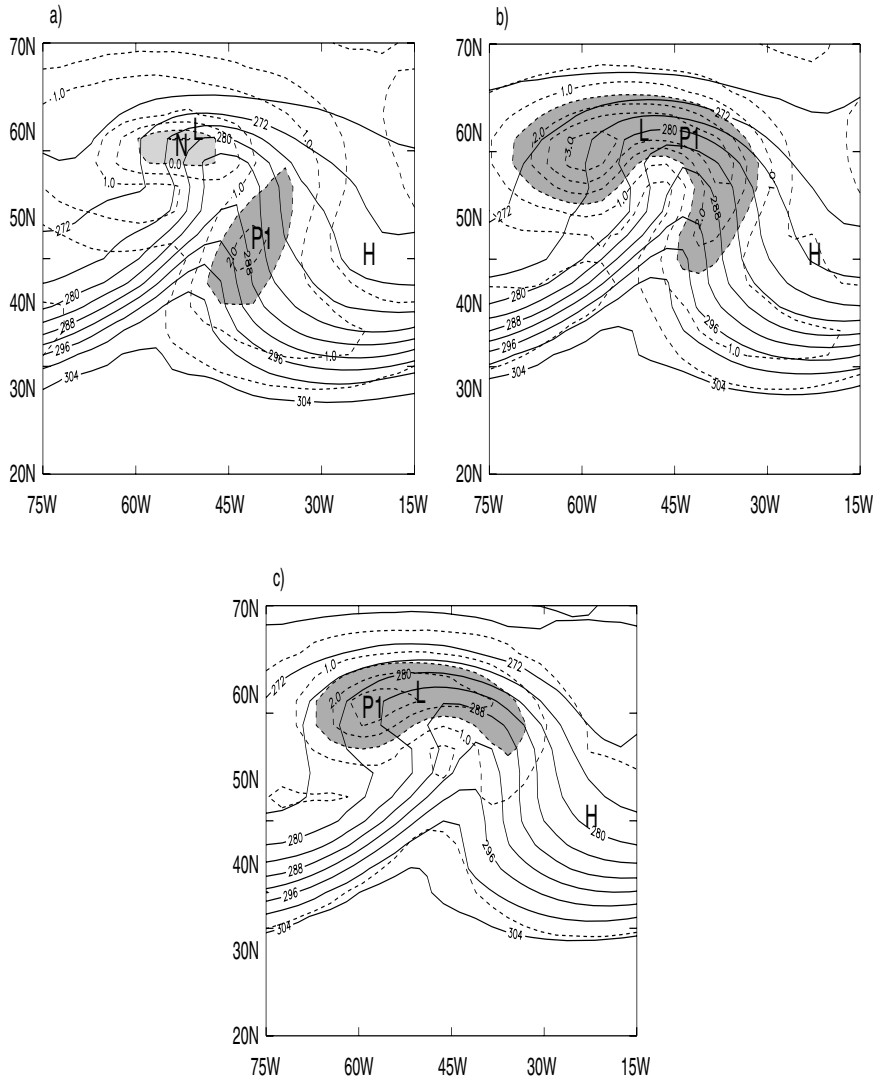

Figure 5. Potential temperature (solid, contour interval 4 K) and potential vorticity (dashed, contour interval 0.5 PVU) in run Rd after six days on the surfaces (a) $\sigma = 0.98$, (b) $\sigma = 0.955$ and (c) $\sigma = 0.92$. PV values >1.5 PVU and <0 PVU are indicated by darker and lighter shading, respectively. L and H denote the surface low and high pressure centres, and locations N and P1 are described in the text.

along the main frontal band, to the east of the source region for the positive anomaly P1 described above. It is possible that the source of P2 is associated with flow around the nearby high centre, and to some extent, therefore, it may arise from the representation of a complete baroclinic wave in these simulations.

As the cyclone enters its decay phase, the WCB becomes more difficult to discern, but the basic characteristics of the main positive PV anomaly P1 are retained until around the tenth day. At the same time, the P2 anomaly does strengthen somewhat but remains a relatively minor feature. Following decay, it is interesting to observe that a positive low-level anomaly is retained in the form of a strip of lower-tropospheric PV. The PV varies little within the strip which occupies a latitude band from $\sim$50° to $\sim$70°N

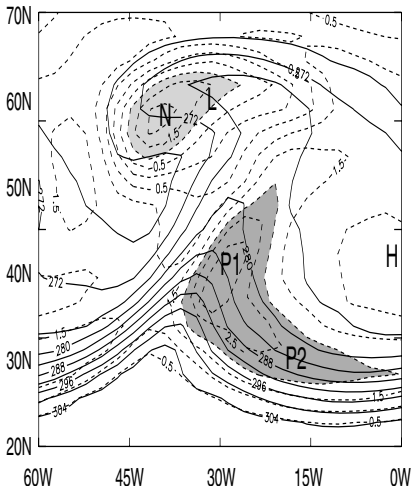

Figure 6. Potential temperature (solid, 4 K contour intervals) and potential vorticity (dashed, 0.5 PVU contour intervals) in run Rd after eight days on the surface $\sigma = 0.98$. PV values >1.5 PVU and <-1 PVU are indicated by darker and lighter shading, respectively. L and H denote the surface low and high pressure centres, and locations N and P1 are described in the text.

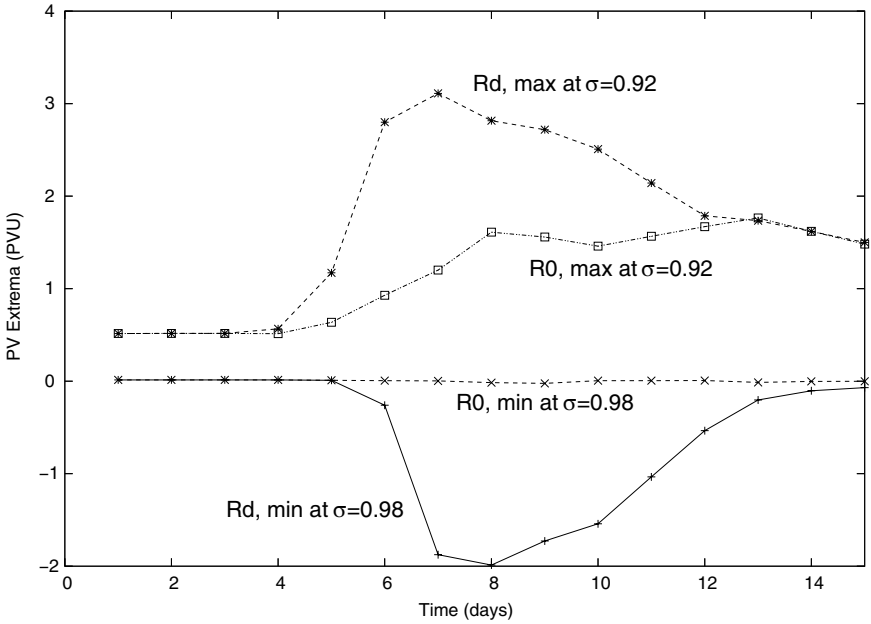

Figure 7. Time series of extreme values of potential vorticity during the life cycles R0 and Rd. Maximum values are shown for the surface $\sigma = 0.92$ and minimum values for the surface $\sigma = 0.98$.

and lies between $\sigma \sim 0.9$ and ~ 0.7 in the vertical. The strip is associated with enhanced static stability (see section 6).

In the remainder of the paper, we ascertain the mechanisms responsible for the low-level PV anomalies described above, and discuss their effects on cyclone development. In doing so, it is assumed that the anomalies are produced through the action of the boundary-layer scheme in run Rd. We have tested this assumption by making

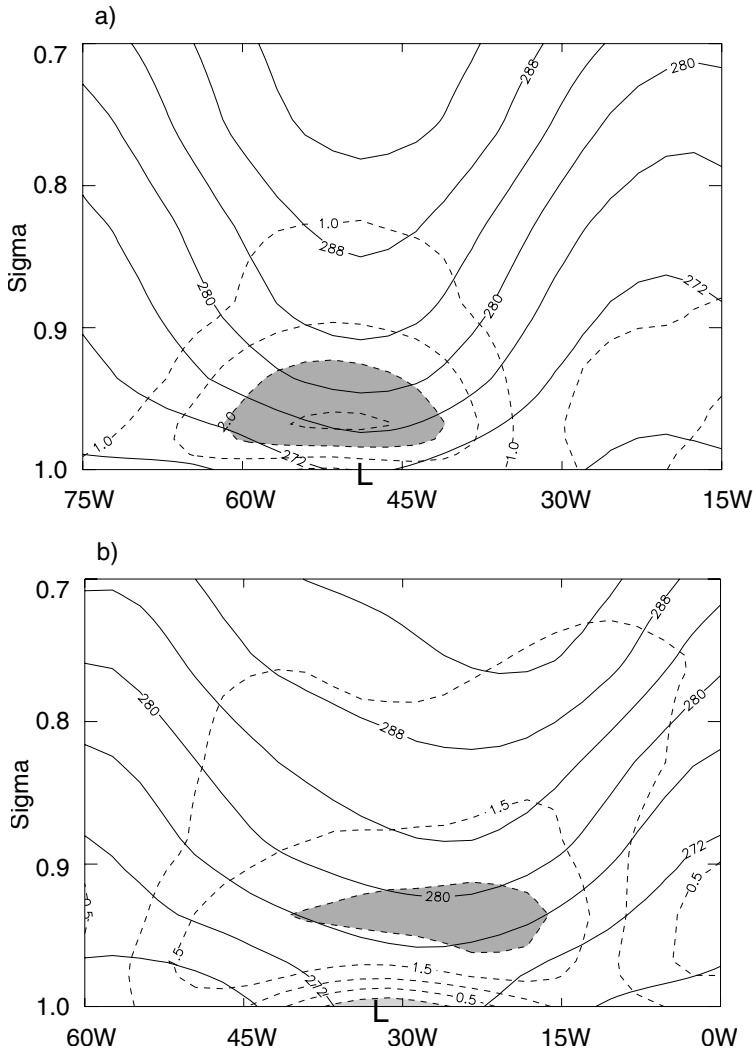

Figure 8. East–west cross-sections of potential temperature (solid, contour interval 4 K) and potential vorticity (dashed, contour interval 0.5 PVU) after (a) six and (b) eight days of run Rd. PV values >2 PVU are shaded. The latitudes chosen, specifically 61° and 64°N for (a) and (b) respectively, are a little north of the surface low centre, whose longitude is marked by L.

comparisons with the run R0, which, apart from numerical effects, is frictionless and adiabatic. In each case, there are positive anomalies formed in both the warm and cold frontal regions. However, in R0, anomalies only become discernible after around seven days (see Fig. 7), when numerical diffusion during occlusion occurs (cf. Nakamura and Held 1989), lifting isentropes at the lower boundary and thereby releasing PV from the surface reservoir. The positive anomaly produced in R0 is considerably smaller both in size and magnitude than that in Rd (Fig. 7), and is not found above the boundary layer. Note also from Fig. 7 that a negative anomaly is not produced in run R0. Thus, our results support the arguments of Cooper *et al.* (1992) that boundary-layer dynamics are considerably more important in producing low-level PV than occlusion caused by the large-scale dynamics.

Finally, the anomalous PV which can be attributed to the numerics in these IGCM runs would appear to have little impact on the eddy evolution. The equivalent R0 simulation evolves similarly when performed with an isentropic model (Woollings 2004) which is more effective at conserving PV.

5. Mechanisms of PV generation

For the dry simulations under consideration here, the free troposphere is frictionless and adiabatic. Thus, the interior PV can only be materially changed due to the action of friction within the boundary layer or numerical effects. In this section, we identify the particular physical processes responsible for the production of the low-level anomalies described above.

(*a*) *Boundary layer PV budget*

It follows from the equations of motion (Hoskins *et al.* 1985) that

$$\mathrm{D}P/\mathrm{D}t = G \equiv \rho^{-1}\nabla \times \mathbf{F} \cdot \nabla\theta, \tag{8}$$

where G is used to represent the PV generation, $\mathbf{F}$ is the frictional force and a diabatic term has been omitted. Following Cooper *et al.* (1992), it is useful to consider the depth-averaged rate of generation, $[G]$, where the square-bracket notation is defined by

$$[A] \equiv h^{-1} \int_0^h A \, \mathrm{d}z, \tag{9}$$

and h is the boundary-layer depth. Some straightforward algebra allows the depth-averaged form of Eq. (8) to be written as

$$\frac{\overline{\mathrm{D}}[P]}{\overline{\mathrm{D}t}} = [G] - \frac{w_h P_h}{h} + \frac{P_h}{h}\left.\frac{\mathrm{D}}{\mathrm{D}t}\right|_h h - \frac{1}{h}\frac{\partial h}{\partial t}[P] - \frac{1}{h}\nabla_{\mathrm{H}} h \cdot [\mathbf{v}_{\mathrm{H}} P], \tag{10}$$

where w is the vertical velocity. This equation characterizes the net effect of drag on the bulk boundary-layer PV, $[P]$. We have neglected a term proportional to $\nabla \cdot \mathbf{v}$ and used the subscript H to denote horizontal components; a subscript h denotes evaluation at $z = h$. The Lagrangian-like derivative operators are also restricted to the horizontal directions, and are suitable for fields $A(x, y)$ defined at a particular height, so that:

$$\left.\frac{\mathrm{D}A}{\mathrm{D}t}\right|_z = \frac{\partial A}{\partial t} + \mathbf{v}_{\mathrm{H}}(z) \cdot \nabla_{\mathrm{H}} A; \tag{11}$$

or else for depth-averaged fields, $[A](x, y)$, for which:

$$\frac{\overline{\mathrm{D}}[A]}{\overline{\mathrm{D}t}} = \frac{\partial [A]}{\partial t} + \nabla_{\mathrm{H}} \cdot [\mathbf{v}_{\mathrm{H}} A]. \tag{12}$$

A simple scale analysis shows that, in the absence of orography, the terms in the budget of Eq. (10) that are proportional to derivatives of the boundary-layer height—the last three terms on the right-hand side—are generally small. (This statement has been confirmed by direct evaluation of the terms from the simulation results.) Therefore, changes to the depth-averaged boundary layer PV are governed by the first two terms: the averaged frictional generation and the flux of PV out of the layer (the flux dictating changes to the net PV in the free troposphere).

(*b*) *Frictional PV generation*

The generation of PV, G, can be decomposed into two components: an *Ekman* component G_{E} and a *baroclinic* component G_{B}, associated respectively with the vertical and horizontal gradients of potential temperature.

As in Cooper *et al.* (1992), we scale the frictional force by the surface stress, writing

$$\mathbf{F} = \frac{\boldsymbol{\tau}_{\mathrm{s}}}{\rho}\frac{\partial S}{\partial z}, \tag{13}$$

so that S is a stress-profile shape factor. This yields

$$[G] = [G_{\mathrm{E}}] + [G_{\mathrm{B}}] = \widehat{\mathbf{k}} \cdot \nabla \times \boldsymbol{\tau}_{\mathrm{s}}\left[\frac{1}{\rho^2}\frac{\partial \theta}{\partial z}\frac{\partial S}{\partial z}\right] + \widehat{\mathbf{k}} \times \boldsymbol{\tau}_{\mathrm{s}} \cdot \left[\frac{1}{\rho^2}\nabla_{\mathrm{H}}\theta\frac{\partial^2 S}{\partial z^2}\right] + \cdots, \tag{14}$$

where $\widehat{\mathbf{k}}$ is the unit vertical vector. The unwritten terms depend either on density variations within the boundary layer, or else on second derivatives of S with respect to both the vertical and a horizontal direction. The physical interpretation of Eq. (14) is greatly simplified by assuming the stress to decay linearly over the depth of the boundary layer. Factors such as $\partial^2 S/\partial x \partial z$ are then proportional to $\partial h/\partial x$ and can be seen to be small. Also neglecting variations of density, then the two terms written explicitly above are the only ones to survive and take particularly simple forms*:

$$[G] = \frac{1}{\rho^2 h^2}\{-\Delta\theta\widehat{\mathbf{k}} \cdot \nabla \times \boldsymbol{\tau}_{\mathrm{s}} + \widehat{\mathbf{k}} \times \boldsymbol{\tau}_{\mathrm{s}} \cdot (\nabla_{\mathrm{H}}\theta)_h\}. \tag{15}$$

Here $\Delta\theta = \theta(h_+) - \theta(0_+)$ is the potential temperature difference across the boundary layer, $\theta(h_+)$ being just above any boundary-layer inversion and $\theta(0_+)$ the air temperature just above the surface.

The first term in Eq. (15), $[G_{\mathrm{E}}]$, is proportional to the temperature jump across the boundary layer, and so is weak for neutral layers and proportional to the inversion strength for well-mixed convective boundary layers. The term is also proportional to the curl of the wind stress, which itself is proportional to the vertical Ekman pumping velocity, w_{E}. Hence, this term can be written as

$$[G_{\mathrm{E}}] = -\frac{f\,\Delta\theta}{\rho h^2} w_{\mathrm{E}}, \tag{16}$$

and is the direct analogue in PV terms of the Ekman spin-down of vorticity in a barotropic vortex. For such a vortex it describes the frictional reduction of vorticity (both directly and through the secondary Ekman circulation; see section 1) as well as the action of the secondary circulation in lifting isentropes, thereby increasing the stability at the top of the boundary layer. For confirmation of the character of the vorticity change we use Eq. (1) to decompose the wind-stress curl as follows:

$$\frac{1}{\rho}\widehat{\mathbf{k}} \cdot \nabla \times \boldsymbol{\tau}_{\mathrm{s}} = C_{\mathrm{D}}|\mathbf{v}|\xi + C_{\mathrm{D}}\left(\frac{v\partial|\mathbf{v}|}{\partial x} - u\frac{\partial|\mathbf{v}|}{\partial y}\right) + |\mathbf{v}|\left(v\frac{\partial C_{\mathrm{D}}}{\partial x} - u\frac{\partial C_{\mathrm{D}}}{\partial y}\right), \tag{17}$$

where ξ is the relative vorticity and we have again neglected density variations in the boundary layer. Direct evaluation using the IGCM results confirms an expectation that the first term in Eq. (17) is dominant. Thus, the sign of the Ekman term $[G_{\mathrm{E}}]$ is such that

* Neglecting factors of ρ this agrees with Eq. (20) of Cooper *et al.* (1992), who assumed a constant density of 1 kg m^{-3}.

ascent by Ekman pumping in a region of cyclonic vorticity will act to reduce both $[P]$ and the vorticity itself. In practice, whether a PV anomaly is predominantly associated with anomalous vorticity or stability will depend upon the shape of the anomaly and its induced flow.

The second term in Eq. (15), $[G_B]$, represents baroclinic generation of $[P]$. It arises from the vorticity in the vertical wind shear and baroclinic temperature gradients just above the boundary layer. Now, according to thermal wind balance, there is a thermal wind just above the boundary layer given by $\mathbf{v}_T \propto \widehat{\mathbf{k}} \times \nabla_H \theta_h$. Furthermore, the surface wind, $\mathbf{v}_s$, is parallel to the surface stress (Eq. (1)). It follows that $[G_B]$ depends upon the orientation of the surface and thermal winds (Cooper *et al.* 1992):

$$[G_B] \propto -\mathbf{v}_s \cdot \mathbf{v}_T = -|\mathbf{v}_s||\mathbf{v}_T| \cos \alpha. \tag{18}$$

If these winds have components in opposing directions, then $[P]$ is generated. Indeed, the near-surface structure of a baroclinic wave does have these winds oriented favourably for generation to occur, as we demonstrate in section 5(c) and discuss further in section 5(d).

It is instructive to consider the magnitude of the baroclinic generation term relative to the Ekman term. From Eq. (15) we have

$$\frac{[G_B]}{[G_E]} \sim \frac{|\nabla_H \theta||\cos \alpha||\boldsymbol{\tau}_s|}{\Delta\theta|\nabla \times \boldsymbol{\tau}_s|}. \tag{19}$$

Taking the leading term from the decomposition of wind-stress curl (Eq. (17)), and estimating the relative vorticity in that term as $\sim \mathbf{v}/L$ yields

$$\frac{[G_B]}{[G_E]} \sim \frac{L|\nabla_H \theta|}{\Delta\theta}|\cos \alpha|. \tag{20}$$

Thus, the ratio of generation terms can be expressed as the product of an angular factor with a ratio of potential temperature differences—that across the horizontal length L of the cyclone to that across the boundary layer. Typical values are $\sim$25 K in the horizontal (see Fig. 2 for example) and $\sim$5 K across the boundary layer (see Fig. 8), giving a ratio of $\sim$5. The angular factor will tend to reduce the ratio and relates to the orientation of surface and thermal winds, an issue we return to in section 5(d). That aside, however, the scaling leads us to anticipate baroclinic PV generation as a prominent feature of the boundary-layer dynamics.

(*c*) *PV generation in* Rd

In this section we ascertain the mechanisms responsible for producing the PV anomalies described in section 4 by computing the PV generation terms obtained above. Our concerns are with the locations of significant PV generation and the relative magnitudes of the generation terms. Therefore, exact calculations of the budget are not necessary. Nor are they warranted, given the approximations made in the derivation of Eq. (15). In this spirit, rather than devising methods to estimate the boundary-layer height at each point (which would require interpolation between model levels), a simple approach is preferred. The expressions in Eq. (15) are evaluated with the boundary layer taken to extend up to the level $\sigma = 0.92$.

A significant low-level PV anomaly becomes apparent after around four days of the run Rd (section 4), with positive PV being produced ahead of the developing cyclone, where the surface fronts are forming (P1 in Fig. 4). The instantaneous PV generation at this time can be seen in Fig. 9. There is destruction of PV due to $[G_E]$

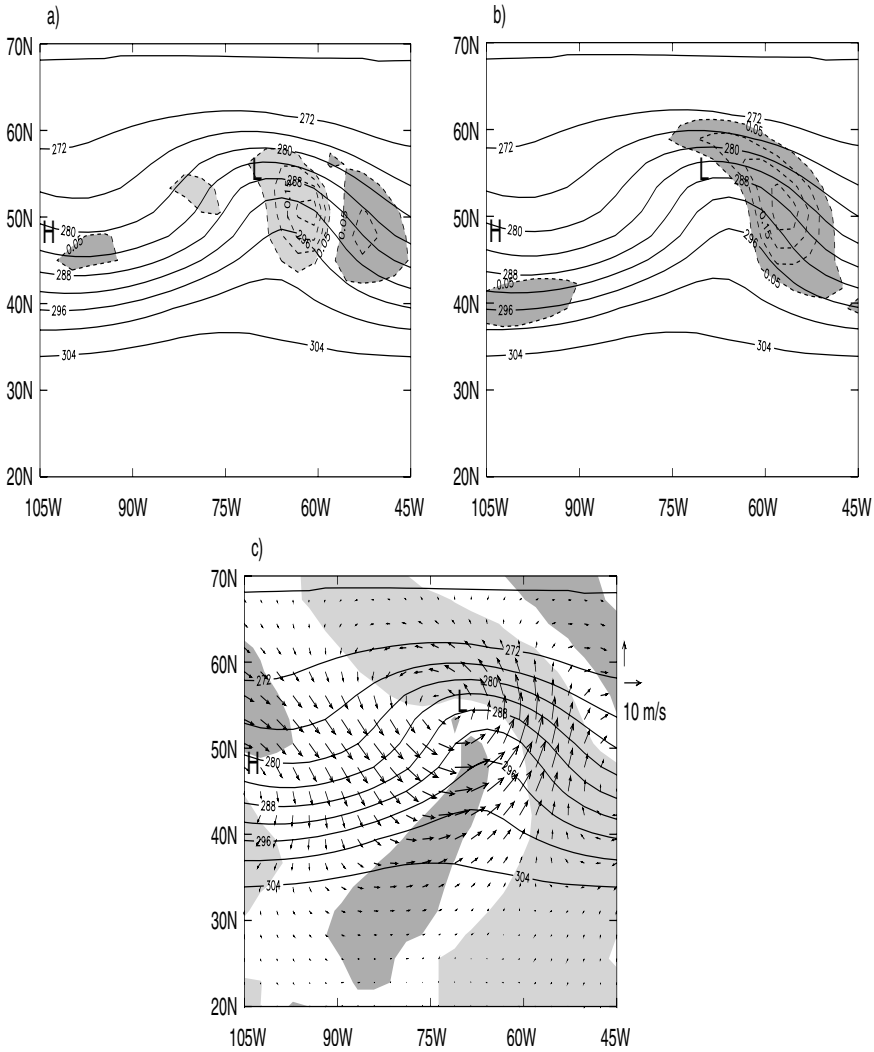

Figure 9. Depth-averaged frictional generation of potential vorticity (dashed, contour interval 0.05 PVU day^{-1}) after four days of run Rd from (a) the Ekman generation term, and (b) the baroclinic generation term. Nearest-neighbour boxcar smoothing has been applied. The zero contour has been suppressed and generation rates >0.05 PVU day^{-1} are shaded, with a darker (lighter) shading for positive (negative) values. In (c), velocity vectors on the surface $\sigma = 0.995$ are plotted, with the scale indicated at the top right. The shading marks regions of significant $\cos\alpha$, where the angle α between the near-surface and thermal winds satisfies $\pi/4 \leqslant \alpha \leqslant 0$ (darker shading) or $3\pi/4 \leqslant \alpha \leqslant \pi$ (light shading). Also shown in each case is the potential temperature (solid, contour interval 4 K) on the surface $\sigma = 0.92$. L and H denote the surface low and high pressure centres.

around the crest of the wave (Fig. 9(a)). It is strongest just ahead of the low centre, in a region with developing cyclonic vorticity and where the boundary-layer stability is strengthening as warm southerly air begins to overrun relatively cool near-surface air. $[G_{\mathrm{E}}]$ generates some PV ahead of the wave, where the vorticity is anticyclonic. The positive PV anomaly P1 is seen to be due to $[G_{\mathrm{B}}]$ on the eastern flank (Fig. 9(b)), with some reinforcement by the positive $[G_{\mathrm{E}}]$. As shown in Fig. 9(c), the region of baroclinic generation is associated with strong surface winds, a developing thermal gradient and a favourable orientation of surface and thermal winds. In no other region of

Fig. 9(c) are all three factors present. In particular, behind the low centre we find strong north-westerly flow across a thermal gradient, but there the surface and thermal winds are close to perpendicular. We consider the physical reasons for the sign and location of significant baroclinic PV generation in section 5(d).

As the cyclone and its associated fronts develop, the regions of frictional PV generation grow both in magnitude and spatial extent. After six days, Fig. 10(a) shows that $[G_{\mathrm{E}}]$ remains at its most intense along the warm conveyor belt, to the east of the low centre. The Ekman mechanism also destroys PV over the low itself. Since $[G_{\mathrm{B}}]$ is predominantly positive, the negative PV anomaly N near the surface close to the low centre (section 4) must be produced by $[G_{\mathrm{E}}]$. The PV anomaly appears over the low itself because of differential advection of the low and the main region of PV destruction. Downstream motion of the low centre is controlled by the large-scale dynamics, and is governed by the steering-level flow at $\sigma \sim 0.7$. Boundary-layer friction, however, means that low-level features are sensitive to the local as well as the large-scale flow in the damped wave. In particular, the Ekman destruction region is located where friction turns the boundary-layer winds towards the low centre against the large-scale flow and so this region is carried downstream a little more slowly than the low itself.

Positive generation of PV continues to occur through $[G_{\mathrm{B}}]$ (Fig. 10(b)), strengthening the P1 anomaly, particularly in the arc where the warm conveyor belt overruns the warm front (cf. Fig. 2). The PV generated is then transported in the fashion described in section 4, ascending to the top of the boundary layer and the lower part of the free troposphere as it is carried north-eastwards along the WCB. This interpretation is confirmed by Fig. 10(c) which shows the PV flux across the top of the boundary layer (i.e. the second term from the right-hand side of Eq. (10)). Subsequent motion is westwards relative to the system, as the WCB turns cyclonically, so a positive anomaly is formed above the low. In comparison with this ascent of the positive anomaly in the WCB, the Ekman pumping velocity is rather small (the WCB dominates the ascent seen in Fig. 2(a)) and so the negative PV anomaly remains confined within the boundary layer.

It is clear from Fig. 10 that there is some overlap between the main regions of baroclinic PV generation and Ekman generation and destruction. The net effect is to concentrate the actual changes to boundary-layer PV along the northern and southern flanks respectively of the generation and destruction regions.

In the further development of the life cycle, the cold front continues to strengthen but the warm frontal gradient slackens somewhat (Thorncroft *et al.* 1993). Moreover, at later times the orientation of surface and thermal winds is unsuitable for further strengthening of the main positive PV anomaly, but these winds do become favourably aligned just behind the cold front. As a result, another generation region develops towards the southern end of the cold front. (An early hint of this region can be seen after six days in Fig. 10(b) at ~35°N, 70°W.) However, the anomalous PV that is produced along this part of the cold front as the low reaches maturity is rather modest.

To summarize, boundary-layer friction has two main influences on the low-level PV. Ekman generation is negative just ahead of the low, weakening the PV and vorticity. This process is therefore consistent with the simple view that friction weakens the low-level flow. However, on the eastern flank of the developing low, positive PV is produced by baroclinic generation, with some reinforcement by Ekman generation. This PV is advected north-eastwards and upwards along the WCB ahead of the surface cold front, is fluxed into the free troposphere, and is then further advected westwards relative to the system, towards the low centre. The result is a positive PV anomaly just above the boundary layer.

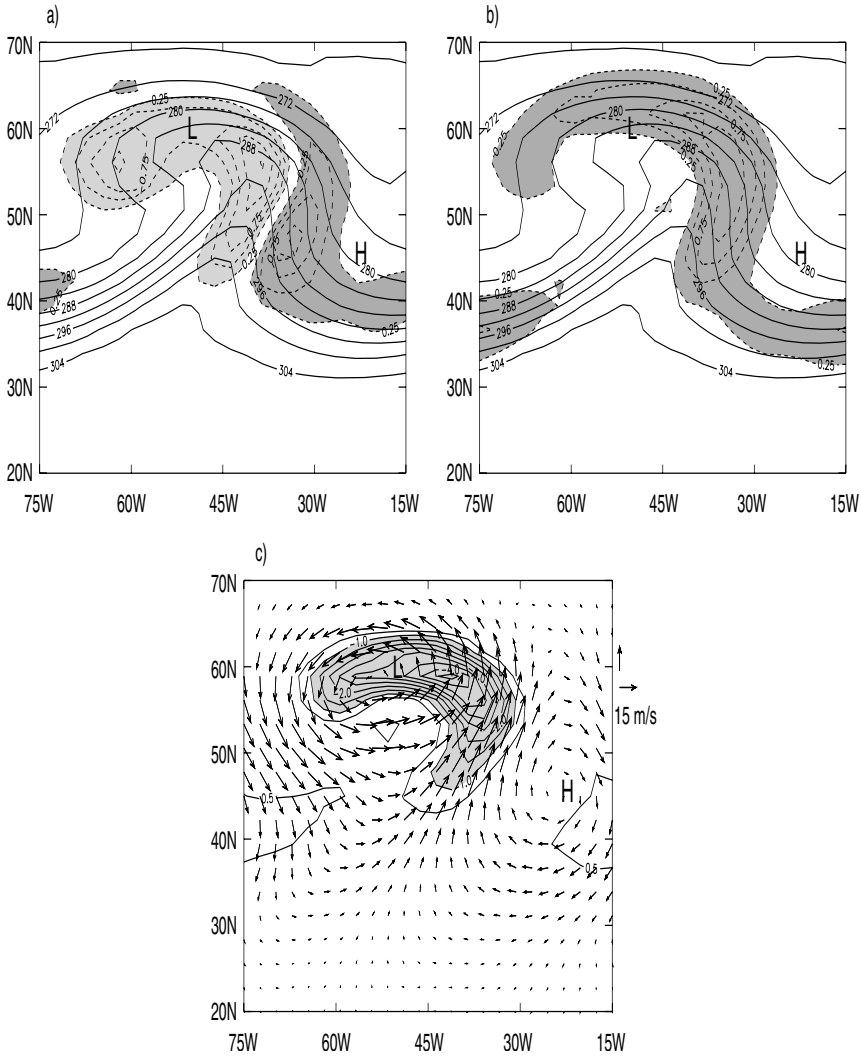

Figure 10. Depth-averaged frictional generation of potential vorticity (dashed, contour interval 0.25 PVU day^{-1}) and PV flux at the top of the boundary layer (solid, contour interval 0.5 PVU day^{-1}) after six days of run Rd: (a) shows the Ekman generation term, (b) the baroclinic generation term and (c) the flux at the top of boundary layer, negative values indicating fluxes out of the layer. Nearest-neighbour boxcar smoothing has been applied to the generation terms, and the zero contour suppressed in each case. Also shown in (a) and (b) is the potential temperature (solid, contour interval 4 K) on the surface $\sigma = 0.92$. Also shown in (c) are velocity vectors on the surface $\sigma = 0.92$ with the scale indicated at the top right. In (a) and (b), generation rates >0.25 PVU day^{-1} are shaded, with a darker (lighter) shading for positive (negative) values. In (c), fluxes >1 PVU day^{-1} are shaded. L and H denote the surface low and high pressure centres.

(*d*) *Baroclinic PV generation*

In section 5(b), it was proposed that friction alters low-level PV, and hence cyclone development, primarily through a baroclinic mechanism. The proposal is supported by the results of section 5(c), which show the baroclinic term to be a significant source of PV in the Rd life-cycle simulation. The impact of that PV on cyclone development is addressed in section 6. Here we consider the character of the baroclinic mechanism within a baroclinic wave.

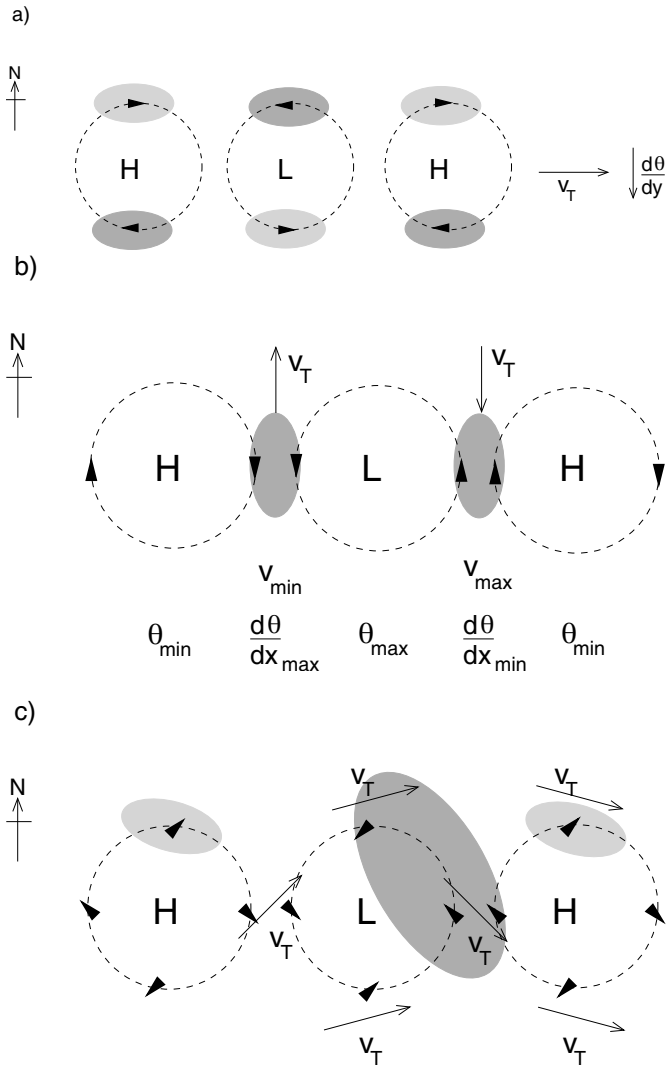

Figure 11. Schematic describing the frictional generation of potential vorticity by the baroclinic mechanism in the linear phase of a baroclinic wave. (a) and (b) illustrate the baroclinic mechanism in a neutral wave associated with the meridional and zonal potential temperature gradients, respectively. (c) illustrates the impact of frictional turning of the wind in a growing wave, with both components of baroclinicity taken into account. L and H denote the surface low and high pressure centres, the arrowheads denote low-level winds and the long arrows denote the thermal wind that is associated with the relevant component(s) of baroclinicity. Shading indicates regions where $\mathbf{v}_S \cdot \mathbf{v}_T$ is large, with darker shading being used for negative values (corresponding to positive baroclinic PV generation). See text for further explanation.

Our discussion follows Fig. 11 and some supporting mathematical argument can be found in appendix A. Figures 11(a) and (b) illustrate those regions suitable for baroclinic PV generation in a neutral wave, as a consequence of meridional and zonal baroclinicity respectively. The impacts of frictional turning of the wind are considered in Fig. 11(c) for both components of the baroclinicity in a growing wave.

As shown in Fig. 11(a), as the basic-state thermal wind is westerly, the zonal wind perturbations imply negative and positive $\mathbf{v}_S \cdot \mathbf{v}_T$ to the north and south of a surface low.

For a high, the signs are reversed. From Eq. (18), this implies a positive PV source north of the low and a negative one to the south. The source is linear in the perturbation strength, being proportional to $U\Lambda$, where Λ is the vertical shear in the basic-state zonal wind and U is a typical amplitude of the zonal wind perturbation.

Now consider the zonal baroclinicity induced in the presence of a baroclinic wave. For a neutral mode, as shown in Fig. 11(b), the thermal wave is out of phase with the pressure wave. Therefore, the meridional wind associated with the wave and the associated thermal wind are perfectly negatively correlated. Hence, in the presence of friction there is positive baroclinic PV generation both ahead of and behind the surface low. As shown in appendix A, for a growing wave, the thermal wave is shifted to the east by an angle ϕ with tangent $\mathrm{Im}(s)/\{\mathrm{Re}(s) - \overline{u}\}$. Here s is the complex-valued phase speed and $\overline{u}$ the basic-state zonal wind. For a typical wave $\mathrm{Im}(s) \sim 3$ m s^{-1} and the relative flow near the surface is ~ 10 m s^{-1}, so that the shift is moderate, typically 15 to 20°. Thus, a strong negative correlation is retained, implying predominantly positive PV generation. The positive generation is centred $\phi/2$ to the east of the maximum northerly and southerly winds, and much weaker negative generation occurs just ahead of the low and high. The magnitude of the negative baroclinic PV generation is typically ~ 50 times smaller than the positive generation. Note that this source term, associated with the induced zonal baroclinicity, is clearly of second order in the wave amplitude, and from appendix A its magnitude is proportional to $V^2\Lambda/\{\mathrm{Re}(s) - \overline{u}\}$, where V is a typical amplitude of the meridional wind. Since V is usually at least as large as U, then this quadratic source can be expected to dominate over the linear source when the winds in the low exceed about 10 m s^{-1}, a relatively small magnitude.

Friction reduces the magnitude and produces a turning of the surface wind, towards the low and away from the high. The turning has a subtle but nonetheless important effect on baroclinic PV generation through its impact on the relative orientation of the surface and thermal winds, as illustrated in Fig. 11(c). For a neutral wave, the meridional wind ahead of the low is turned to have a westward component. Since this component opposes the basic eastward thermal wind, this implies an increase in the positive PV source there. Behind the low, however, the turning of the southward flow in the direction of the basic-state thermal wind means that the positive source there is reduced. For a neutral wave, turning of the maximum and minimum westerly winds on the meridional flanks of the pressure systems produces no additional source of PV there.

For a growing wave, there is no change in the impact of the turning of the meridional winds to the east and west of the low. However, as is evident in Fig. 11(c), there is now a small impact through the turning of the zonal winds. To the north of the high and low, the respective negative and positive sources are enhanced, whereas to the south of the pressure systems the sources are reduced.

Combining all these arguments, the expectation in a system with winds of order 10 m s^{-1} or greater is for the baroclinic PV source to exhibit a dominant positive generation to the east and north-east of the low. The arguments given are consistent with the orientation of the surface and thermal winds after four days in the life-cycle experiment described here (Fig. 9(c)) and the structure of the baroclinic generation seen (Fig. 9(b)). At later times, the thermal and surface winds change their character somewhat, but Fig. 10(b) suggests that the generic arguments presented in this section remain a good guide to the PV generation. These arguments are thought to be applicable quite generally to midlatitude weather systems. It is notable that the turning of the wind plays a vital role in the distribution and magnitude of baroclinic PV generation, and in particular in the major source being to the east, rather than the west, of the low.

6. A MECHANISM FOR REDUCED BAROCLINIC WAVE GROWTH

The normal mode theory of baroclinic wave development describes the cooperative interaction of Rossby waves, one on the lower surface and the other located chiefly near the steering level and the tropopause (Methven *et al.* 2004). The interaction, and hence the growth rate, is mediated by the interior static stability. Thus, in the 2D frontal model of Nakamura and Held (1989), PV fluxed into the interior from the boundaries at the point of occlusion reduced baroclinic growth rates, owing to an associated increase in stability. A similar argument applies to the results of this study.

The generation and advection of positive boundary-layer PV results in a band of anomalously high PV in the region of the low centre. Figure 8 shows vertical cross-sections through this positive anomaly, which is associated with enhanced stability, as can be seen from the spacing of potential temperature contours. By definition, the positive anomaly of PV must be associated with either a cyclonic vorticity anomaly or a positive static-stability anomaly. According to Hoskins *et al.* (1985), the partitioning of a PV anomaly into contributions from vorticity and static-stability anomalies depends upon the shape of the anomaly. A tall, narrow anomaly is attributable mainly to increased vorticity, while a broad, flat anomaly is mostly attributable to increased static stability. In this case, the anomaly spreads in the horizontal and remains confined in the vertical. The spreading occurs because of westward advection of the anomaly in the cyclonic branch of the WCB, combined with an increasing zonal separation between the main frictional PV source and the low centre. Ekman transport in the vicinity of the low centre also contributes to the redistribution of PV and the evolution of the positive anomaly. Ekman pumping produces isentropic lifting which decreases the static stability within the boundary layer itself, whilst increasing it just above. Also associated with the uplift is divergence above the boundary layer, which enhances the horizontal spreading (Xu *et al.* 1998).

The stability anomaly is produced despite the fact that the generation of PV is by frictional processes. Thus a geostrophic adjustment process must take place, analogous to the adjustment associated with localized latent heating in the mid-troposphere. In that case the adjustment has the opposite sense, diabatically generated PV anomalies above and below the heating being partially transformed into vorticity anomalies.

As well as reducing wave development, the stability anomaly will act to inhibit subsequent baroclinic developments and contribute to the stabilization of the atmosphere by the eddy. As noted in section 4, a PV/static-stability anomaly in the lower troposphere persists beyond eddy decay (Fig. 12). The stabilization is often thought of in terms of the action of the eddy in reducing baroclinicity (Simmons and Hoskins 1978; see also Zurita-Gotor and Lindzen (2004) for a recent discussion). From Fig. 12, this is manifest in run R0 by warming of the troposphere at latitudes from 50° to 70°N. The stronger eddy with stronger low-level flow means that (particularly in the lower troposphere) run R0 is more effective at warming these latitudes than Rd. However, the residual static-stability anomaly in Rd at least provides some compensation in the overall stabilization and indeed raises the question of whether frictional damping of eddies has a net positive or negative effect in this regard.

Based on the averaged stability between the fourth and eighth days (Adamson 2001), we can use Eady's growth equation to make a simple-minded estimate of the reduction in baroclinic growth rate, r, due to the static-stability anomaly. From Gill (1982),

$$r = \frac{\mathrm{d}\overline{u}}{\mathrm{d}z_*}\frac{fk[q(\coth q + \tanh q) - 1 - q^2]^{1/2}}{N_*\sqrt{k^2+\ell^2}}; \quad q = \frac{D}{2H_\mathrm{R}} = \frac{fD}{2N_*\sqrt{k^2+\ell^2}}. \qquad (21)$$

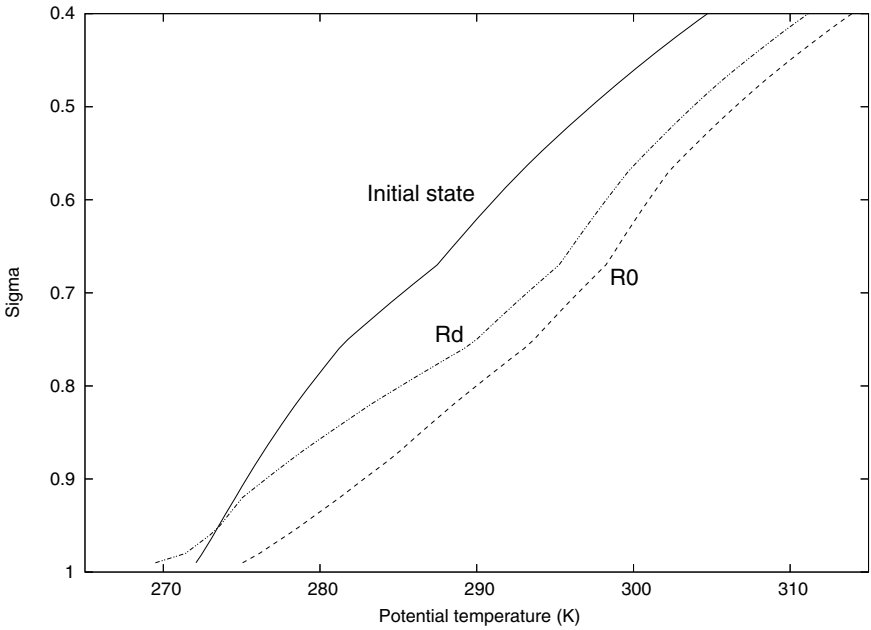

Figure 12. Profiles of the zonal-mean potential temperature averaged between latitudes 50° and 70°N, for the initial state (solid) and for runs R0 (dashed) and Rd (dotted), averaged between 15 and 20 days.

Here $\overline{u}$ is the basic-state zonal wind, k and ℓ are wave numbers in the zonal and meridional directions, N is the buoyancy frequency, D is the depth of the troposphere and a $*$ subscript denotes the use of log-pressure vertical coordinates. This suggests a reduction by $\sim$40%, of which $\sim$25% is a direct effect of increased stability (the $1/N_*$ factor in Eq. (21)) whereas $\sim$15% arises because the wave-number-six eddy becomes a sub-optimal perturbation at the increased Rossby radius of deformation (i.e. increased H_{R} leads to a reduction in the factor in square brackets in Eq. (21)). Not least because the stability anomaly becomes significant during the nonlinear phase of growth, such an estimate cannot be viable as a quantitative prediction. Nonetheless, it is sufficient to make the point that the enhancement to low-level stability is strong enough to have a considerable impact on the evolution of the frictionally damped baroclinic wave.

7. Conclusions

Previous studies of surface drag in 3D baroclinic cyclogenesis have tended to concentrate either on the detailed behaviour of the boundary layer itself (Doyle 1995; Lionello *et al.* 1998) or on the modifications to the large-scale energetics (e.g. Jones 1992). Here, we have performed dry baroclinic life-cycle simulations with the IGCM and considered the dynamical mechanisms through which surface drag influences the interior cyclone structure and how this then changes cyclone development.

The dominant effect of drag has generally been assumed to be Ekman transport, a mechanism which reduces the intensity of a barotropic vortex by vortex squashing. This is clearly a generic process within frictionally damped cyclones, the associated negative PV generation requiring only a cyclonic vorticity and boundary-layer stability. Although we do indeed find evidence for the action of this mechanism, it does not take account of important baroclinic processes within a midlatitude cyclone. The PV framework reveals a distinct baroclinic mechanism (first described by Cooper *et al.* (1992)

and subsequently discussed by Davis *et al.* (1993) and Stoelinga (1996)). This also has a generic status, requiring only baroclinicity and a non-perpendicular alignment of the surface and thermal winds. Simple arguments indicate that the associated changes in PV will be predominantly positive, will be concentrated to the east and north-east of a surface low (section 5(d)) and will be stronger than those from the Ekman mechanism (section 5(b)).

The IGCM simulation results show that positive PV is indeed baroclinically generated to the north and east of the low centre as the frontal regions develop. There is also some Ekman generation ahead of the low associated with anticyclonic vorticity. At later times, the region of frictional generation extends southwards ahead of the cold front as well as to the north and east of the bent-back warm front. The generated positive PV is fluxed out of the boundary layer into the free troposphere by the large-scale ascending flow along the warm conveyor belt. The PV is then transported westwards towards the low centre, leading to a large, positive PV anomaly above the boundary layer over the surface low. Isentropic lifting caused by Ekman transport and the associated divergence above the boundary layer contribute to the shape of this anomaly, which is confined in the vertical, but has a large horizontal extent. As a result, the PV anomaly is associated with a large, positive static-stability anomaly. It is this anomalously high static stability that leads to a reduction in baroclinic growth.

Reduced baroclinic growth produces a cyclone that equilibrates later and with lower intensity when surface drag is included in the life cycle (section 3). Note also that the PV and static stability anomalies persist in the lower troposphere during the decay phase of the life cycle and so will act to stabilize the atmosphere to subsequent baroclinic developments.

Finally, we remark that these results may have important implications for the forecasting of extratropical storms. Storm development is known to be particularly sensitive to subsynoptic-scale PV perturbations near to the fronts or close to the steering level (Beare *et al.* 2003), locations in which the frictionally generated anomalies were found.

Acknowledgements

D. Adamson acknowledges funding from a NERC studentship. R. Plant acknowledges funding from the UWERN programme, supported by NERC. We are grateful to A. Beljaars for providing us with information about the mixing-length boundary-layer schemes that have been used by ECMWF. We also thank M. Blackburn for assistance with the numerical model and useful discussions of his own work on baroclinic frictional generation of PV. Finally, we wish to acknowledge constructive comments received from the referees.

Appendix A

Mathematics of baroclinic PV generation

This appendix supplements the discussion of section 5(d) by providing some supporting mathematical details.

Consider a basic-state flow with zonal wind $\overline{u}$ and potential temperature $\overline{\theta}$, and a normal mode perturbation with structure proportional to $\exp\{\mathrm{i}k(x - st)\}$, where s may be complex. At the lower boundary, for which $w = 0$, the perturbation potential temperature θ' satisfies

$$(\overline{u} - s)\frac{\partial \theta'}{\partial x} = -v'\frac{\partial \overline{\theta}}{\partial y}. \tag{A.1}$$

Using the thermal wind relation for both the basic state and the perturbation, this implies

$$(\overline{u} - s)\frac{\partial v'}{\partial z} = v'\Lambda, \tag{A.2}$$

where $\Lambda = \partial\overline{u}/\partial z$ is the basic-state shear.

For positive Λ, the relative flow at the surface is always westward (e.g. Bretherton 1966). Therefore, letting $\widetilde{u} = \mathrm{Re}(s) - \overline{u}$, with $\widetilde{u}$ positive, Eq. (A.2) becomes

$$\frac{\partial v'}{\partial z} = -\frac{v'}{\widetilde{u} + \mathrm{i}\,\mathrm{Im}(s)}\Lambda. \tag{A.3}$$

Hence, $-\partial v'/\partial z$ leads the v' wave on the lower boundary by an angle

$$\phi = \tan^{-1}\left\{\frac{\mathrm{Im}(s)}{\widetilde{u}}\right\}. \tag{A.4}$$

Also from Eq. (A.3), consider the product $-v'\partial v'/\partial z$, which is proportional to the quadratic contribution to baroclinic PV generation. This has minima and maxima that occur respectively at $\phi/2$ ahead of the zeros and extrema of v'. The ratio of magnitudes for the negative to positive extrema in the product is $\tan^2(\phi/2)$. Thus, the negative extrema in the product are smaller than the positive ones for all $\widetilde{u}$ and s.

For a neutral wave, $\mathrm{Im}(s) = 0$ and the phase difference ϕ vanishes. For the most unstable Eady wave, $\mathrm{Im}(s)/\widetilde{u} \approx 0.38$, so that ϕ is about 21°. Taking a typical midlatitude e-folding time of 1.5 days for a wavelength of 2500 km gives $\mathrm{Im}(s) \sim 3$ m s^{-1}, whereas $\widetilde{u}$ is typically $\sim$10 m s^{-1}, giving a phase difference of $\sim$17°. The modest phase difference means that the above ratio of magnitudes for the extrema in $-v'\partial v'/\partial z$ is small, in this example $\sim$0.02.

REFERENCES

Adamson, D. S. 2001 'The effects of frictional processes in baroclinic cyclogenesis'. PhD thesis, Department of Meteorology, University of Reading, UK

Arya, S. P. 1988 *Introduction to micrometeorology.* Academic Press

Beare, R. J., Thorpe, A. J. and White, A. A. 2003 The predictability of extratropical cyclones: Nonlinear sensitivity to localized potential-vorticity perturbations. *Q. J. R. Meteorol. Soc.*, **129,** 219–237

Belcher, S. E. and Hunt, J. C. R. 1998 Turbulent flow over hills and waves. *Annu. Rev. Fluid Mech.*, **30,** 507–538

Beljaars, A. C. M., Brown, A. R. and Wood, N. 2004 A new parameterization of turbulent orographic form drag. *Q. J. R. Meteorol. Soc.*, **130,** 1327–1347

Blackadar, A. K. 1962 The vertical distribution of wind and turbulent exchange in a neutral atmosphere. *J. Geophys. Res.*, **97,** 3095–3102

Bretherton, F. P. 1966 Baroclinic instability and the short wavelength cut-off in terms of potential vorticity. *Q. J. R. Meteorol. Soc.*, **92,** 335–345

Browning, K. A. and Roberts, N. M. 1994 Structure of a frontal cyclone. *Q. J. R. Meteorol. Soc.*, **120,** 1535–1557

Card, P. A. and Barcilon, A. 1982 The Charney stability problem with a lower Ekman layer. *J. Atmos. Sci.*, **39,** 2128–2137

Cooper, I. M., Thorpe, A. J. and Bishop, C. H. 1992 The role of diffusive effects on potential vorticity in fronts. *Q. J. R. Meteorol. Soc.*, **118,** 629–647

Davis, C. A., Stoelinga, M. T. and Kuo, Y.-H. 1993 The integrated effect of condensation in numerical simulations of extratropical cyclogenesis. *Mon. Weather Rev.*, **121,** 2309–2330

Doyle, J. D. 1995 Coupled ocean wave/atmosphere mesoscale model simulations of cyclogenesis. *Tellus*, **47A,** 766–778

ECMWF Research Department 1991 'ECMWF forecast model: physical parameterization'. Research manual 3 (3rd ed.) ECMWF, Reading, UK

ECMWF Research Department 2002 'IFS documentation. Part IV: Physical processes (CY25R1)'. Ed. P. W. White. ECMWF, Reading, UK

Farrell, B. 1985 Transient growth of damped baroclinic waves. *J. Atmos. Sci.*, **42,** 2718–2727

Gill, A. E. 1982 *Atmosphere-ocean dynamics.* Academic Press

Haynes, P. H. and McIntyre, M. E. 1987 On the evolution of vorticity and potential vorticity in the presence of diabatic heating and friction or other forces. *J. Atmos. Sci.*, **44,** 828–841

Holton, J. R. 1992 *An introduction to dynamic meteorology* (3rd ed.) Academic Press

Hoskins, B. J. and Simmons, A. J. 1975 A multi-layer spectral model and the semi-implicit method. *Q. J. R. Meteorol. Soc.*, **101,** 637–655

Hoskins, B. J., McIntyre, M. E. and Robertson, A. W. 1985 On the use and significance of isentropic potential vorticity maps. *Q. J. R. Meteorol. Soc.*, **111,** 877–946

Janssen, P. A. E. M. 1989 Wave-induced stress and the drag of airflow over sea waves. *J. Phys. Oceanogr.*, **19,** 745–754

1991 Quasi-linear theory of wind wave generation applied to wave forecasting. *J. Phys. Oceanogr.*, **21,** 1631–1642

Jones, B. 1992 'Effects of physical processes in baroclinic waves'. PhD thesis, Department of Meteorology, University of Reading, UK

Lionello, P., Malguzzi, P. and Buzzi, A. 1998 Coupling between the atmospheric circulation and the ocean wave field: An idealized case. *J. Phys. Oceanogr.*, **28,** 161–177

Lott, F. and Miller, M. J. 1997 A new subgrid-scale orographic drag parametrization: Its formulation and testing. *Q. J. R. Meteorol. Soc.*, **123,** 101–127

Louis, J. F. 1979 A parametric model of vertical eddy fluxes in the atmosphere. *Boundary-Layer Meteorol.*, **17,** 187–202

Louis, J. F., Tiedtke, M. and Geleyn, J. F. 1982 'A short history of the operational PBL parameterization at ECMWF'. Pp. 59–79 in Proceedings of Workshop on planetary boundary-layer parameterization, 25–27 November 1981. ECMWF, Reading, UK

Methven, J. 1996 'Tracer behaviour in baroclinic waves'. PhD thesis, Department of Meteorology, University of Reading, UK

Methven, J., Heifetz, E., Hoskins, B. J. and Bishop, C. H. 2005 The counter-propagating Rossby wave perspective on baroclinic instability. III: Primitive-equation disturbances on the sphere. *Q. J. R. Meteorol. Soc.*, **131,** 1393–1424

Milton, S. F. and Wilson, C. A. 1996 The impact of parameterized subgrid-scale orographic forcing on systematic errors in a global NWP model. *Mon. Weather Rev.*, **124,** 2023–2045

Nakamura, N. and Held, I. M. 1989 Nonlinear equilibration of two-dimensional Eady waves. *J. Atmos. Sci.*, **46,** 3055–3064

Schneider T., Held I. M. and Garner, S. T. 2003 Boundary effects in potential vorticity dynamics. *J. Atmos. Sci.*, **60,** 1024–1040

Simmons, A. J. and Hoskins, B. J. 1978 The lifecycles of some nonlinear baroclinic waves. *J. Atmos. Sci.*, **35,** 414–432

1980 Barotropic influences on the growth and decay of nonlinear baroclinic waves. *J. Atmos. Sci.*, **37,** 1679–1684

Stoelinga, M. T. 1996 A potential vorticity-based study on the role of diabatic heating and friction in a numerically simulated baroclinic cyclone. *Mon. Weather Rev.*, **124,** 849–874

Thorncroft, C. D., Hoskins, B. J. and McIntyre, M. E. 1993 Two paradigms of baroclinic-wave life-cycle behaviour. *Q. J. R. Meteorol. Soc.*, **119,** 17–55

Valdes, P. J. and Hoskins, B. J. 1988 Baroclinic instability of the zonally averaged flow with boundary layer damping. *J. Atmos. Sci.*, **45,** 1584–1593

Viterbo, P., Beljaars, A. C. M., Mahfouf J.-F. and Teixeira J. 1999 The representation of soil moisture freezing and its impact on the stable boundary layer. *Q. J. R. Meteorol. Soc.*, **125,** 2401–2426

Wood, N. and Mason, P. J. 1993 The pressure force induced by neutral, turbulent flow over hills. *Q. J. R. Meteorol. Soc.*, **119,** 1233–1267

Woollings, T. J. 2004 'Entropy and potential vorticity in dynamical core atmosphere models'. PhD thesis, Department of Meteorology, University of Reading, UK

Xu, Q., Gu, W. and Gao, J. D. 1998 Baroclinic Eady waves and fronts. Part 1: Viscous semigeostrophy and the impact of boundary conditions. *J. Atmos. Sci.*, **55,** 3598–3615

Zurita-Gotor, P. and Lindzen, R. S. 2004 Baroclinic equilibration and the maintenance of the momentum balance. Part II: 3D Results. *J. Atmos. Sci.*, **61,** 1483–1499